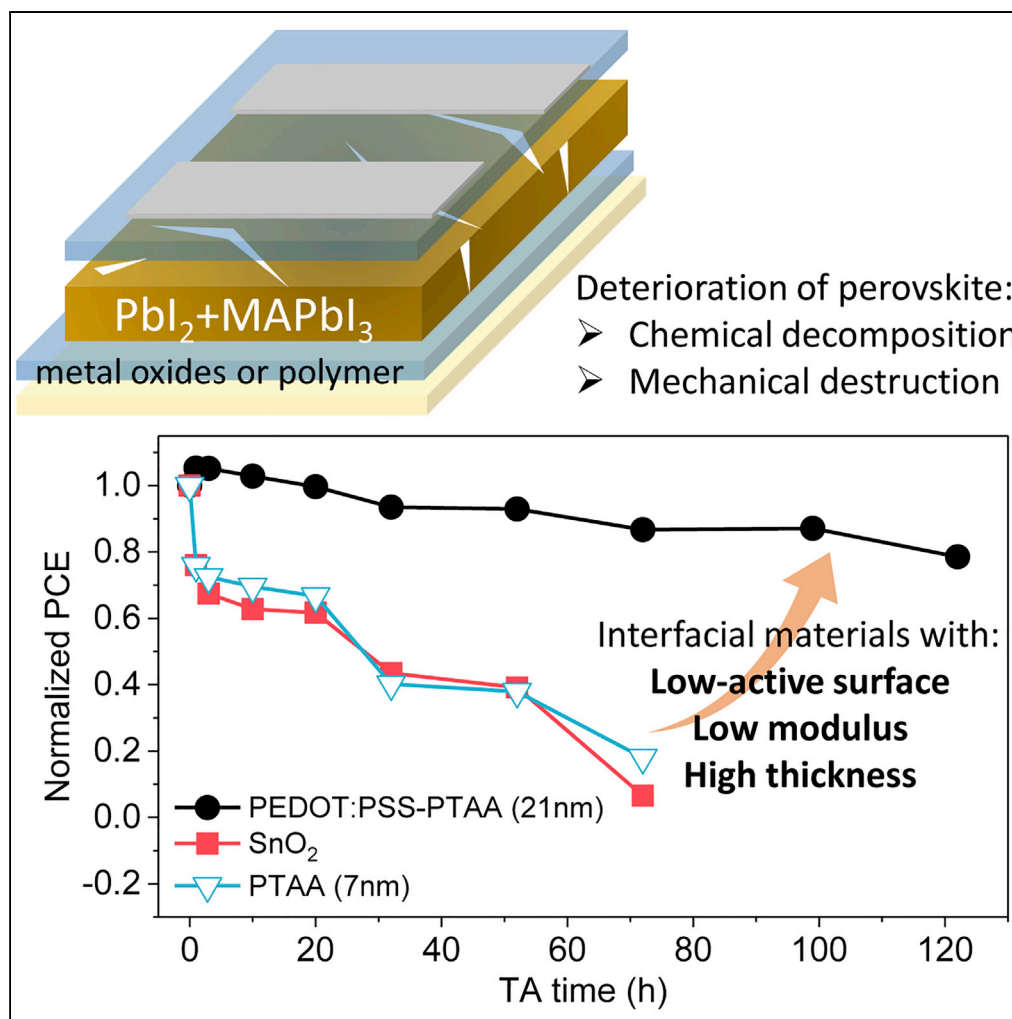


## Article

# Toward Highly Thermal Stable Perovskite Solar Cells by Rational Design of Interfacial Layer



Weitao Yang,  
Danming Zhong,  
Minmin Shi,  
Shaoxing Qu,  
Hongzheng Chen

squ@zju.edu.cn (S.Q.)  
hzchen@zju.edu.cn (H.C.)

### HIGHLIGHTS

Degradation of perovskite films on different substrates were studied

The chemical and mechanical deterioration of perovskite films are distinguished

Thermal-induced stress within PVSCs was eased by a soft and thick interfacial layer

PVSCs with optimized interfacial layers showed superior thermal stability

## Article

# Toward Highly Thermal Stable Perovskite Solar Cells by Rational Design of Interfacial Layer

Weitao Yang,<sup>1</sup> Danming Zhong,<sup>2</sup> Minmin Shi,<sup>1</sup> Shaoxing Qu,<sup>2,\*</sup> and Hongzheng Chen<sup>1,3,\*</sup>

## SUMMARY

Heat is crucial to the long-term stability of perovskite solar cells (PVSCs). Herein, thermal stability of PVSCs based on metal oxide (MO) and polymer (P) was investigated. Firstly, chemical decomposition behavior of perovskite films was characterized and analyzed, revealing that chemically active MO would accelerate the decomposition of methylamine lead iodide (MAPbI<sub>3</sub>). Secondly, thermal-induced stress, resulting from the mismatched thermal expansion coefficients of different layers of PVSCs, and its effect on the mechanical stability of perovskite films were studied. Combining experiment and simulation, we conclude that “soft” (low modulus) and thick (>20 nm) interfacial layers offer better relaxation of thermal-induced stress. As a result, PVSCs employing thick polymer interfacial layer offer a remarkably improved thermal stability. This work offers not only the degradation insight of perovskite films on different substrates but also the path toward highly thermal stable PVSCs by rational design of interfacial layers.

## INTRODUCTION

Perovskite solar cells (PVSCs) based on halide lead perovskite such as methylamine lead iodide (MAPbI<sub>3</sub>) have emerged as one of the most promising candidates for solar energy harvest due to their outstanding photo-electronic properties and compatibility to large-area solution-processing fabrication. Nowadays, the power conversion efficiency (PCE) of the state-of-the-art PVSCs has been over 23% with small-area, and over 15% with large-area (Jiang et al., 2019a; Jung et al., 2019; Deng et al., 2018; Li et al., 2018). Instability of PVSCs, therefore, becomes the major bottleneck for their commercial applications. In the last decade, degradation mechanism of perovskite absorber as well as the over-roll device has been widely studied. Heat, illumination, moisture, and oxygen are considered to be the four most essential environmental factors that are responsible for deterioration of PVSCs (Boyd et al., 2019; Deretzi et al., 2018; Askar et al., 2017). Generally, the degradation of PVSCs is triggered by moisture and oxygen and would be accelerated under illumination or high temperature conditions (Askar et al., 2017; Bi et al., 2016; Juarez-Perez et al., 2016). Among them, moisture and oxygen issues could be tackled by hermetic encapsulation, which would also greatly reduce the negative influence of illumination (Jiang et al., 2019b; Han et al., 2015). However, it is reported that photovoltaic modules operating in hot climate could reach temperature of 65°C or even higher, and high temperature processes (such as annealing of device layer and device encapsulation) are involved in PVSCs fabrication (Boyd et al., 2019; Tress et al., 2019). On one hand, chemical and crystal phase deterioration of perovskite films would occur under thermal stress. Methods including perovskite ions engineering, defects passivation, and device engineering have been fully developed to achieve PVSCs with better thermal stability (Jiang et al., 2019a; Turren-Cruz et al., 2018; Bian et al., 2018; Niu, et al., 2018; Wang et al., 2019; Chen et al., 2018). On the other hand, thermal-induced built-in stress would form within the PVSCs due to the mismatched thermal expansion coefficients of different layers in device (Rolston et al., 2018a, 2018b; Jacobsson et al., 2015). Huang and his co-workers have reported a strain-accelerated degradation of perovskite film under illumination because of the increased ion migration (Zhao et al., 2017). What is more, a low toughness of <0.16 MPa m<sup>0.5</sup> (comparable to that of NaCl crystal, which is 0.15–0.26 MPa m<sup>0.5</sup>) of perovskite crystal has been reported (Rolston et al., 2016; Ramirez et al., 2018). As a result, sufficient stress would accumulate within the device when operating under extreme temperature and thus induce fracture. However, few attention has been paid on tackling such thermal-induced stress. Fabricating PVSCs based on polymer substrates such as polyethylene terephthalate (PET) instead of glass seems to be an alternative approach to reduce such built-in stress (Zhao et al., 2017; Hu et al., 2019). But their inferior moisture/oxygen blocking ability and relatively low hardness compared with their inorganic counterparts hold back their further applications. Hence, detailed influences of thermal aging on the PVSCs stability are worth

<sup>1</sup>State Key Laboratory of Silicon Materials, MOE Key Laboratory of Macromolecular Synthesis and Functionalization, Department of Polymer Science and Engineering, Zhejiang University, Hangzhou 310027, P.R. China

<sup>2</sup>State Key Laboratory of Fluid Power & Mechatronic System, Key Laboratory of Soft Machines and Smart Devices of Zhejiang Province, Department of Engineering Mechanics, and Center for X-Mechanics, Zhejiang University, Hangzhou 310027, P.R. China

<sup>3</sup>Lead Contact

\*Correspondence: [squ@zju.edu.cn](mailto:squ@zju.edu.cn) (S.Q.), [hzchen@zju.edu.cn](mailto:hzchen@zju.edu.cn) (H.C.)

<https://doi.org/10.1016/j.isci.2019.11.007>



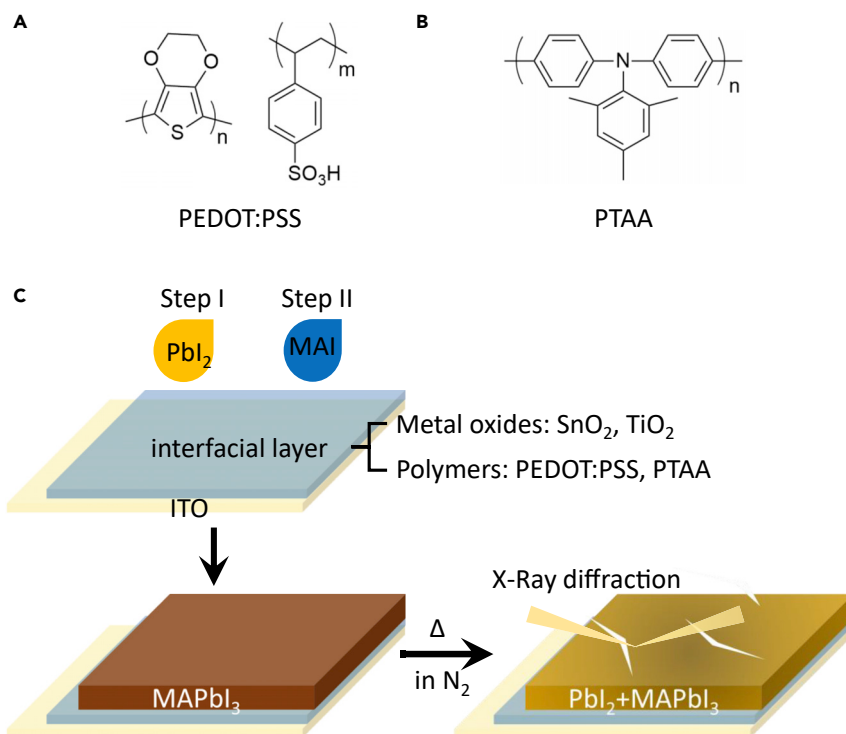


**Figure 1. Molecular Structures and Sample Characterization**

(A and B) The molecular structures of PEDOT:PSS (A) and PTAA (B).

(C) Diagram of MAPbI<sub>3</sub> perovskite preparation on different interfacial layers and their thermal aging testing.

further investigations, and strategies to improve the heat endurance of PVSCs need to be developed to meet the requirement of practical applications.

Herein, thermal stability of perovskite films based on substrates with various interfacial layers of metal oxides and polymers was investigated. Based on the results of X-ray diffraction, optical microscope, etc., the chemical and mechanical origins responsible for the degradation of perovskite films were distinguished. Further mechanics simulation and thermal stability test of full PVSC devices suggest that a thick and soft polymer interfacial layer with low-active surface is preferred for highly thermal stable PVSCs. This work elucidates the influence of interfacial layer properties on the thermal stability of PVSCs, providing a simple route to PVSCs capable for practical use by rational choice of interfacial layer materials.

## RESULTS AND DISCUSSION

### Decomposition of MAPbI<sub>3</sub> under Thermal Aging

ITO glass substrates coated with four different interfacial layers of compact tin oxides (SnO<sub>2</sub>), compact titanium oxides (TiO<sub>2</sub>), poly(3,4-ethylenedioxythiophene):polystyrene sulfonate (PEDOT:PSS Al 4083), and poly[bis(4-phenyl)(2,4,6-trimethylphenyl)amine] (PTAA) were prepared according to the previous reports (Huang et al., 2016; Liu et al., 2018; Yang et al., 2019; Zhou et al., 2014). The molecular structures of PEDOT:PSS and PTAA are presented in Figures 1A and 1B, respectively. Tested by a stylus profiler, the thickness of SnO<sub>2</sub>, TiO<sub>2</sub>, PEDOT:PSS, and PTAA layers is determined to be 30 nm, 30 nm, 24 nm, and 7 nm, respectively. We choose these four materials not only because they belong to the two most widely used categories (metal oxide and polymer) of interfacial layer materials in PVSCs but also because they represent three mechanical property conditions including “tough and thick” (as SnO<sub>2</sub>, TiO<sub>2</sub>), “soft and thick” (as PEDOT:PSS), and “soft and thin” (as PTAA). These merits enable an ideal platform for us to carry out the study via well-designed trials. MAPbI<sub>3</sub>, one of the most commonly used and well-studied organic-inorganic hybrid perovskites for photovoltaic applications, was then deposited on different interfacial layers via a two-step method (Huang et al., 2016; Kojima et al., 2009; Chen et al., 2017). Details about the experimental conditions could be seen in the Supplemental Information. X-ray diffraction (XRD)

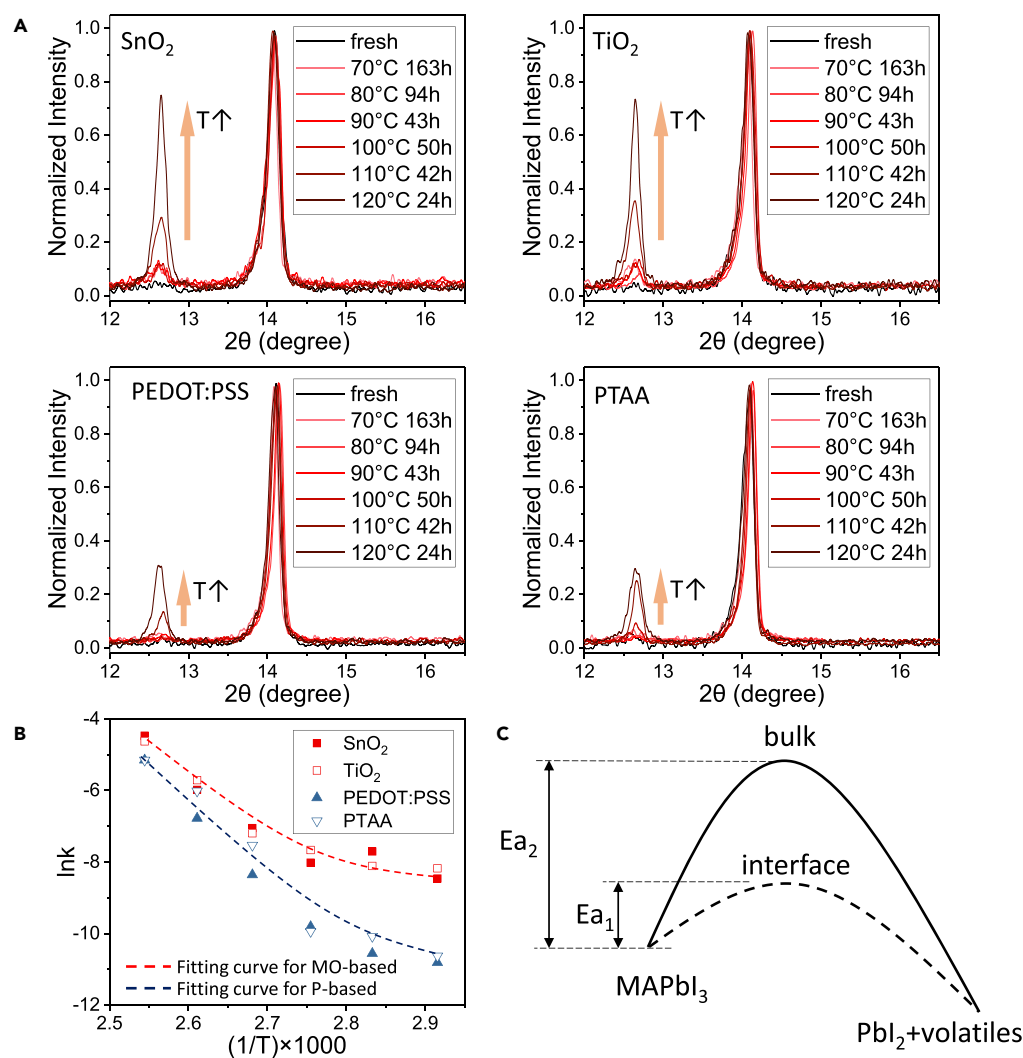


**Figure 2. Chemical Deposition Analysis**

(A) XRD patterns of perovskite films prepared on different substrates after thermal aging on various conditions.

(B) lnk-(1/T) plots of perovskite films on different interfacial layers.

(C) Diagram of decomposition process taking place in bulk (solid line) and in interface (dash line).

Also see Figures S1–S3.

patterns and top-view scanning electron microscope (SEM) images of different fresh perovskite films are shown in Figure S1. No significant difference in crystallinity and morphology is observed, indicating similar perovskite quality on different substrates. Finally, the as-prepared perovskite films were put on hotplate with various temperatures for thermal aging in glove box (see Figure 1C).

X-ray diffraction characterization was performed to examine the decomposition of MAPbI<sub>3</sub> films. As shown in Figure 2A, two peaks corresponding to PbI<sub>2</sub> and MAPbI<sub>3</sub>, respectively, were detected at 12.7° and 14.1° (Zhao et al., 2017). By quantifying the peak area of PbI<sub>2</sub> and MAPbI<sub>3</sub> under various thermal stress, we could determine the decomposition rate (k) of MAPbI<sub>3</sub> by:

$$k = \frac{S_{PbI_2}}{(S_{PbI_2} + b \cdot S_{MAPbI_3}) \Delta t}$$

where  $\Delta t$  is the thermal aging duration and  $S_{PbI_2}$  and  $S_{MAPbI_3}$  are the peak areas of PbI<sub>2</sub> and MAPbI<sub>3</sub>, respectively.  $b = 1.92$  is the calibration factor determined as the ratio of the intensity of PbI<sub>2</sub> (001) plane signal in totally aged perovskite sample to the intensity of MAPbI<sub>3</sub> (110) plane signal in fresh perovskite sample (see

Interfacial Layer	A <sub>1</sub>	E <sub>a1</sub> (kJ/mol)	A <sub>2</sub> × 10 <sup>-20</sup>	E <sub>a2</sub> (kJ/mol)	R <sup>2</sup>
MO-based	0.0595	20.8	3.64	169.7	0.9994
P-based	0.0088	20.8	2.06	169.7	0.9988

**Table 1. Parameters Used to Fit the Experimental  $\ln k$ -(1/T) Data**

Figure S2). Background  $\text{PbI}_2$  signals have been removed by measuring the XRD spectra of the corresponding fresh perovskite films. Different  $k$  values under six different temperatures various from 343K to 393K were then measured and calculated, offering  $\ln k$ -(1/T) curves of perovskite films deposited on different interfacial layers shown in Figure 2B. Depicted in Figure 2B, perovskite films deposited on metal-oxides-based (MO-based) layers ( $\text{SnO}_2$  and  $\text{TiO}_2$ ) suffer from higher decomposition rates than those deposited on polymer-based (P-based) layers (PEDOT:PSS and PTAA). What is more, high  $\ln k$  tails at low temperature range were observed for MO-based perovskite films. Assuming that there are two parallel reactions during the decomposition process, we could fit the  $\ln k$ -(1/T) data according to the Arrhenius equation:

$$k = A_1 e^{-E_{a1}/RT} + A_2 e^{-E_{a2}/RT}$$

where  $A$  and  $E_a$  are the pre-exponential factor and apparent activation energy for each decomposition process,  $R = 8.314 \text{ J}/(\text{mol}\cdot\text{K})$  is the gas constant, and  $T$  is the absolute temperature. Shown in Figure 2B and Table 1, an identical  $E_{a2}$  (169.7 kJ/mol) for MO-based and P-based perovskites was observed at high temperature region, which could be related to the bulk-dominated decomposition of perovskite (Smecca et al., 2016; Yu et al., 2017; Deretzis et al., 2015). This value is also consistent with the previous reported values obtained by different methods (Smecca et al., 2016; Yu et al., 2017; Deretzis et al., 2015). More importantly, the  $A_1$  of MO-based perovskite (0.0595) is  $\sim 6.8$  folds higher than that of the P-based perovskite (0.0088), indicating significant enhancement in lower  $E_a$  ( $E_{a1} = 16.6 \text{ kJ/mol}$ ) process at lower temperature region for MO-based perovskite. Considering the high  $k$  and low  $E_a$  features of this process, we suggest it should be related to the excess decomposition of perovskite catalyzed by residual active species on the MO/perovskite interface. To verify our hypothesis, isonicotinic acid (molecular structure shown in Figure S3 inset), a reported effective interfacial passivation molecule, was employed to prepare a self-assembling monolayer (SAM) on the MO-based substrates (Zuo et al., 2015, 2017). Details about the preparation of

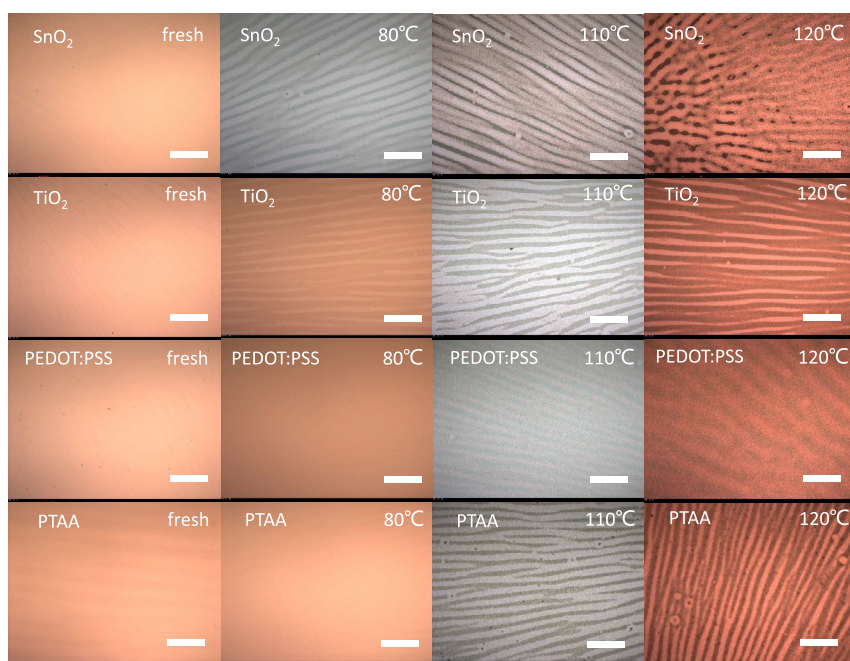


**Figure 3. Optical Microscope Images of Perovskite Films**

Optical microscope images of perovskite films deposited on different interfacial layers under thermal aging with different temperatures. Scale bars in all pictures represent 200  $\mu\text{m}$ .

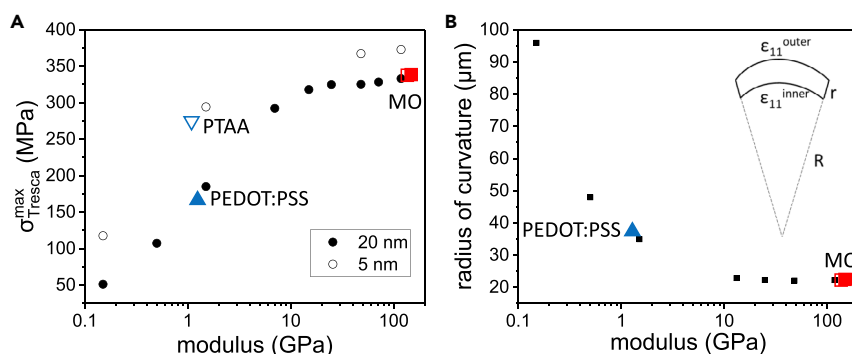


**Figure 4. Mechanics Simulation**

(A) Dependence of max Tresca equivalent stress on the modulus and thickness of interfacial layer under a simulative temperature of 120°C.

(B) Dependence of radius of curvature on the modulus of interfacial layer under a simulative temperature of 120°C. Simulative positions of the interfacial layers employed in this work are marked in the plots.

Also see [Figures S4–S6](#) and [Table S1](#).

SAM could be seen in the [Supplemental Information](#). As a result, the  $k$  value significantly drop from  $-8.2$  for reference substrates to  $-9.4$  for SAM-passivated substrates under thermal stress at 363 K (shown in [Figure S3](#)), which is very close to that of the P-based substrates ( $\ln k = -9.8$ ). Based on these results, we argue that the chemically active MO-based substrates would offer extra interfacial decomposition pathway for perovskite (illustrated in [Figure 2C](#)). P-based interfacial materials with low-activity surface are preferred for PVSCs with better thermal stability.

### Mechanical Fracture of MAPbI<sub>3</sub> Film and Simulation

The influence of thermal aging temperature on the mechanical stability of perovskite films was studied. Researchers have emphasized the impact of mismatched thermal expansion coefficients of different layers in device on the mechanical stability of PVSCs during thermal annealing ([Boyd et al., 2019](#); [Jacobsson et al., 2015](#); [Ramirez et al., 2018](#)). Particularly, the thermal expansion coefficient of MAPbI<sub>3</sub> reaches  $1.57 \times 10^{-4} \text{ K}^{-1}$ , which is six times larger than those of indium tin oxide (ITO) and soda lime glass ([Jacobsson et al., 2015](#); [Fabini et al., 2016](#)). Given the fairly low fracture energy ( $<1.5 \text{ J/m}^2$ ) of perovskite due to its ionic salt-like structure, PVSCs might suffer from significant destruction under intense thermal stress ([Rolston et al., 2018b](#)). Herein, optical microscope was adopted to examine the morphology of perovskite films under various thermal aging conditions. As shown in [Figure 3](#), obvious wrinkling fracture was observed in MO-based perovskite films after thermal annealing at over 80°C for 94 h. Similar destruction of perovskite films could also be seen in perovskite films based on PTAA layer. Considering different chemical decomposition behaviors for MO-based and PTAA-based perovskites discussed in the above section, we ascribe these wrinkles to the mechanical fracture of perovskite films, which is resulted from the thermal-induced compressive stress. It is worth pointing out that perovskite films deposited on PEDOT:PSS interfacial layer possess much less wrinkles even under high temperature over 110°C than that deposited on PTAA and MOs. Considering the thicker (or softer) layer of PEDOT:PSS than PTAA (or MOs), we hypothesize that thickness as well as modulus of the interfacial layer might be essential to the mechanical stability of perovskite film under thermal stress.

To have an in-depth understanding on the mechanical fracture of MAPbI<sub>3</sub> films, we performed finite element simulation based on mechanical properties, and the conditions are summarized in [Table S1](#). Tresca equivalent stress  $\sigma_{Tresca}$  [defined as the maximal difference between principal stresses, i.e.  $\sigma_{Tresca} = \max(|\sigma_1 - \sigma_2|, |\sigma_1 - \sigma_3|, |\sigma_2 - \sigma_3|)$ , with the three principal stresses  $\sigma_1, \sigma_2, \sigma_3$ ], which commonly serves as failure criterion for solid sample, is adopted to characterize the stress levels in the MAPbI<sub>3</sub> layer. Herein, the dependence of maximum Tresca equivalent stress ( $\sigma_{Tresca}^{max}$ ) within the perovskite layer on the modulus ( $E$ ) and the thickness of interfacial layer was simulated. Exhibited in [Figure 4A](#), the higher the modulus of the interfacial layer or the thinner the thickness of the interfacial layer, the higher the  $\sigma_{Tresca}^{max}$  within the perovskite layer. Particular positions corresponding to SnO<sub>2</sub>, TiO<sub>2</sub>, PEDOT:PSS, and PTAA interfacial layer materials are marked in the plot, demonstrating considerably higher  $\sigma_{Tresca}^{max}$  for MO-based ( $\sigma_{Tresca}^{max} > 300 \text{ MPa}$ ) and PTAA-based ( $\sigma_{Tresca}^{max} \approx 280 \text{ MPa}$ ) perovskite films than that of PEDOT:PSS-based perovskite film ( $\sigma_{Tresca}^{max} \approx 160 \text{ MPa}$ ). The higher stress level would lead to more serious destruction within

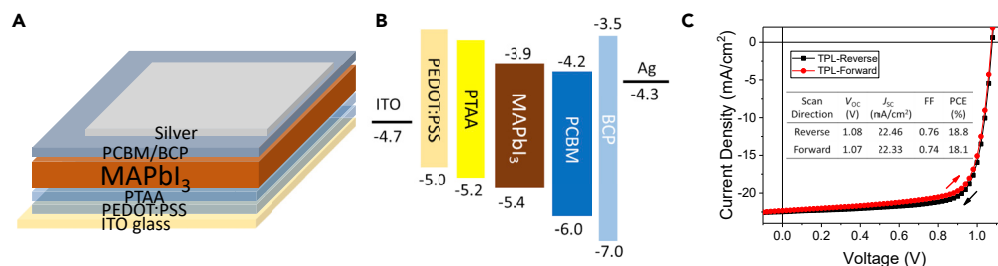


**Figure 5. Device Structure, Energy Level Diagram, and PVSC Performance**

(A) Device structure of TPL-based PVSCs.

(B) Energy level diagram of the PVSCs.

(C) Forward (red) and reverse (black) scanned J-V curves of the champion TPL-based PVSC.

Also see [Tables S2](#) and [S3](#).

the perovskite films, which is consistent with the optical microscope results in [Figure 3](#). In addition, these results imply a threshold fracture stress of between 160 and 280 MPa. This value is consistent on the order of magnitude with the previous reported yield stress ( $\sim 740$  MPa for single crystal perovskite), and tensile fracture stress ( $\sim 130$  MPa for polycrystal perovskite film) of MAPbI<sub>3</sub> perovskite, indicating good validity of this simulation ([Reyes-Martinez et al., 2017](#); [Ahn et al., 2019](#)). In a word, the mechanics simulation suggests significant mechanical buffer effect of the thick and soft interfacial layer, providing reasonable explanation for the alleviated wrinkles of PEDOT:PSS-based perovskite film.

Secondly, due to the constraint effect of substrate on perovskite film, there would be unbalanced thermal expansion across the perovskite films (see [Figure S4](#)). Such distortion of perovskite films are transformed and represented by the equivalent radius of curvature ( $r$ ) determined by  $r = L \times (\epsilon_{11}^{inner} + 1) / (\epsilon_{11}^{outer} - \epsilon_{11}^{inner})$ , where  $L = 300$  nm is the thickness of perovskite film and  $\epsilon_{11}^{outer}$  and  $\epsilon_{11}^{inner}$  are the  $\epsilon_{11}$  (the strain along direction 1) adjacent to the surface and interface, respectively (illustrated in the right top inset of [Figure 4B](#)). The  $r$ - $E$  curve was then depicted in [Figure 4B](#), where a 2–5 folds larger  $r$  was obtained when  $E$  decreases from more than 10 GPa to 0.1–1 GPa, suggesting more intense distortion of perovskite films on tough interfacial layers than those on soft interfacial layers. Finally, mechanics simulation of the full device containing counter electrode (silver) and top interfacial layer ([6,6]-phenyl-C61-butyric acid methyl ester [PCBM]) was performed, demonstrating comparable results (illustrated in [Figure S5](#)). To further prove our simulation result, optical microscope images of perovskite films based on thick PTAA ( $\sim 30$  nm) and thin PEDOT:PSS ( $\sim 8$  nm) after thermal aging were collected. In spite of the low coverage of perovskite films ([Figure S6](#)) due to the bad wettability between PbI<sub>2</sub> solution and PTAA surface, perovskite film based on thick PTAA shows much fewer wrinkling fracture than that on thin PEDOT:PSS after thermal annealing at 110°C ([Figure S6](#)). Based on these results, both experimental and simulative, we argue that a soft (with modulus of few GPa or less) and relatively thick (thickness  $>20$  nm) interfacial layer would effectively release the thermal-induced stress within the PVSCs, contributing to improved thermal stability.

### Related to the PCE Degradation

PVSCs based on different interfacial layers were fabricated to evaluate the relationship between the thermal degradation of MAPbI<sub>3</sub> film and the device performance. As shown in [Table S2](#), the SnO<sub>2</sub>, TiO<sub>2</sub>, PEDOT:PSS-, and PTAA-based PVSCs show the maximum PCEs of 15.26%, 13.55%, 13.56%, and 17.15%, respectively, indicating good charge transporting capability of the above interfacial layers. In order to study the influence of the thickness of polymer interfacial layers on the thermal stability of the PVSCs, we further fabricated PVSCs with device structure of ITO/PEDOT:PSS/PTAA/MAPbI<sub>3</sub>/electron transport layer/Ag, where a bilayer thick polymer layer (TPL) was adopted. Device structure and energy level diagram of such TPL-based PVSCs was shown in [Figures 5A](#) and [5B](#). Optimization of TPL could be seen in [Table S3](#). In brief, higher thickness leads to inferior charge transport capability, resulting in a decreased  $J_{SC}$ , whereas too thin thickness leads to a low  $V_{OC}$ . Finally, the optimized TPL possesses a thickness of  $\sim 21$  nm (with thickness of 14 nm and 7 nm for PEDOT:PSS and PTAA, respectively). Encouragingly, such TPL-based devices show a highest PCE of 18.8% ([Table S2](#)), probably due to the cascade energy level alignment (see [Figure 5B](#)) of ITO/PEDOT:PSS/PTAA/MAPbI<sub>3</sub>, which offer better charge collection efficiency. The J-V curve and parameters of the champion device was depicted in [Figure 5C](#).

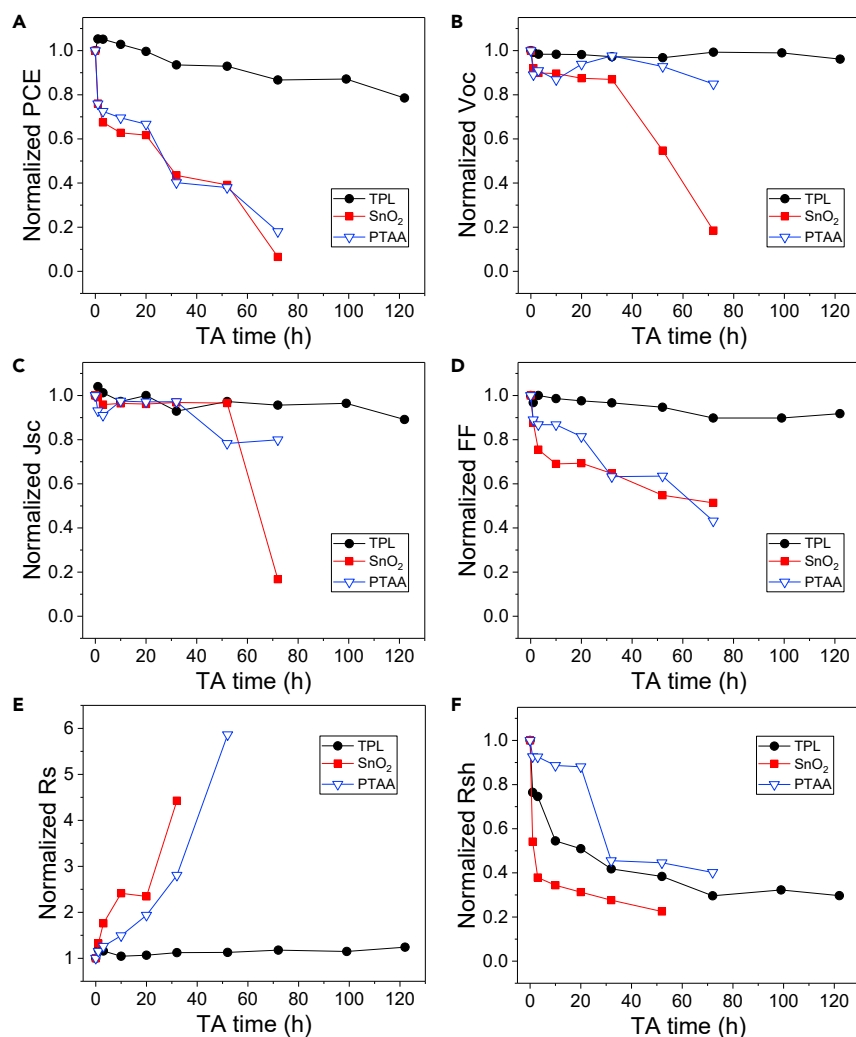


**Figure 6. Device Thermal Stability Test**

(A–F) PCE (A),  $V_{OC}$  (B),  $J_{SC}$  (C), FF (D),  $R_s$  (E), and  $R_{sh}$  (F) evolution of PVSCs based on TPL (black solid circle), SnO<sub>2</sub> (red solid square), and PTAA (blue hollow down triangle) interfacial layers heated at 100°C in glovebox. Also see Figure S7.

Then, PVSCs based on SnO<sub>2</sub> (30 nm), PTAA (7 nm), and PEDOT:PSS/PTAA (21 nm) interfacial layers were fabricated, and their thermal stability were examined by placing different devices on 100°C hotplate in glove box. As shown in Figure 6A, the SnO<sub>2</sub>-based and PTAA-based PVSCs suffer from severe PCE deterioration in the first 24 h, remaining only 40% of their initial PCEs after thermal aging for 40 h. On the contrary, the TPL-based devices keep over 80% of their initial PCEs after over 120 h annealing. By replacing Ag with Au to eliminate the electrode corrosion, the thermal stability could be further improved, offering a T80 of more than 380 h (see Figure S7). Detailed parameters evolution (shown in Figures 6B–6D) indicates that fill factor (FF) decay is the primary factor responsible for the PCE drops. To understand the mechanism of such difference in device performance, sheet resistance ( $R_s$ ) and shunt resistance ( $R_{sh}$ ) evolutions were derived from the corresponding J-V curves and depicted in Figures 6E and 6F. On one hand,  $R_s$  of the SnO<sub>2</sub>-based and PTAA-based devices significantly increased and reached over five folds of their initial values, whereas  $R_s$  of the TPL-based PVSCs barely changed (see Figure 6E). On the other hand, greater decrease in  $R_{sh}$  was observed for SnO<sub>2</sub>-based PVSCs (see Figure 6F). According to the equivalent circuit description of photovoltaics,  $R_s$  is related to the bulk and contact resistance of the device, whereas  $R_{sh}$  is related to the leak current caused by defects or pinholes within the active layer (Wu et al., 2015). Hence, we reasonably attribute the increase in  $R_s$  and the decrease in  $R_{sh}$  to the fracture and decomposition of MAPbI<sub>3</sub> layer according to our finding discussed in the former sections.

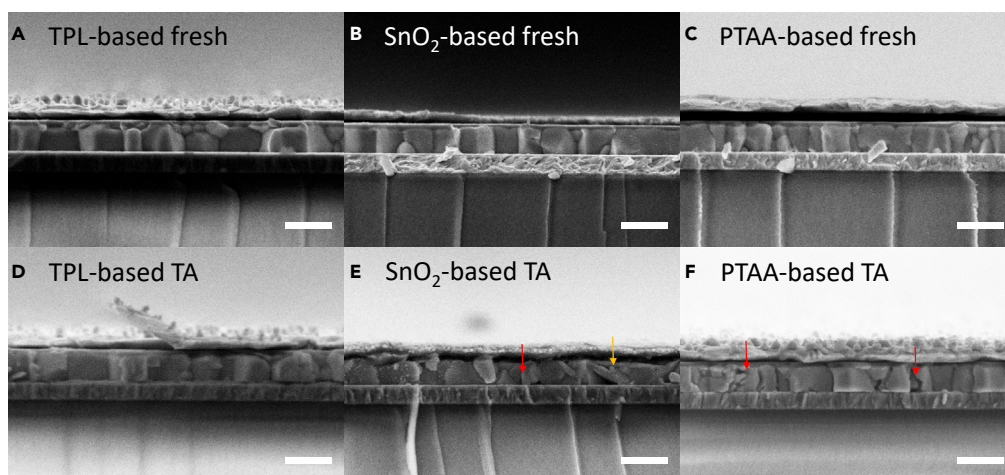


**Figure 7. SEM Cross-Sectional Images of PVSCs**

(A–C) Cross-sectional images of TPL-based PVSC (A), SnO<sub>2</sub>-based PVSC (B), and PTAA-based PVSC (C) before thermal aging. Scale bars in all pictures represent 500 nm.

(D–F) Cross-sectional images of TPL-based PVSC (D), SnO<sub>2</sub>-based PVSC (E), and PTAA-based PVSC (F) after thermal aging at 100°C. Scale bars in all pictures represent 500 nm.

We further verified our argument by conducting the cross-sectional SEM characterization. As shown in Figure 7B, the crystal fracture (marked by red arrow) features were observed in thermal-aged PVSCs based on both PTAA and SnO<sub>2</sub> layers (Figures 7E and 7F), whereas obvious PbI<sub>2</sub> product (flake-like feature marked by yellow arrow) could only be seen in SnO<sub>2</sub>-based PVSCs (Figure 7E). These results also agree well with the XRD characterization where much stronger PbI<sub>2</sub> signal was observed in SnO<sub>2</sub>-based perovskite than in P-based perovskites after thermal aging at 100°C (Figures 1A–1C). In a word, the device performance test and SEM results further support our XRD and optical microscope characterizations and the corresponding conclusions. PEDOT:PSS/PTAA, a thick polymer interfacial layer, exhibits outstanding chemical and mechanical stability under thermal stress.

## Conclusion

In this work, influence of interfacial layer on the thermal stability of perovskite was thoroughly studied. The overall degradation of perovskite was distinguished into chemical decomposition and mechanical fracture via XRD and optical microscope characterizations, etc. Accelerated decomposition and worse mechanical destruction were observed in MO-based perovskite films, which are ascribed to the chemically active surface as well as high modulus feature of metal oxides interfacial layer materials. After conducting mechanics simulation and overall device stability test, we demonstrate the qualities desired for a good interfacial layer, including low modulus (few GPa or less), low chemical activity, and capability of thick layer (thickness >20 nm) utilization. In a word, our work offers not only the degradation insight of the perovskite films based on various substrates but also the path toward PVSCs with good heat endurance by rational design of interfacial layer materials.

## Limitations of the Study

In this study, a thick polymer interfacial layer is adopted to improve the high thermal stability of PVSCs. However, the deterioration of polymeric materials should be carefully considered under other aging conditions.

## METHODS

All methods can be found in the accompanying [Transparent Methods supplemental file](#).

## SUPPLEMENTAL INFORMATION

Supplemental Information can be found online at <https://doi.org/10.1016/j.isci.2019.11.007>.

## ACKNOWLEDGMENTS

This work was supported by the National Natural Science Foundation of China (Grant Nos. 51620105006 and 61721005), Zhejiang Province Science and Technology Key Plan (No. 2018C01047), and International Science and Technology Cooperation Program of China (ISTCP) (Grant No. 2016YFE0102900).

## AUTHOR CONTRIBUTIONS

W. Y. and H. C. conceived the idea and designed the experiments. W. Y. carried out the experiments. D. Z. and S. Q. conducted and analyzed the mechanics simulation. H. C. supervised the project. W. Y., D. Z., M. S., and H. C. analyzed the results and prepared the paper. All authors commented on the paper.

## DECLARATION OF INTERESTS

The authors declare no competing financial interests.

Received: August 12, 2019

Revised: October 6, 2019

Accepted: November 3, 2019

Published: December 20, 2019

## REFERENCES

- Ahn, S.-m., Jung, E.D., Kim, S.-H., Kim, H., Lee, S., Song, M.H., and Kim, J.-Y. (2019). Nanomechanical approach for flexibility of organic-inorganic hybrid perovskite solar cells. *Nano Lett.* *19*, 3707–3715.
- Askar, A.M., Bernard, G.M., Wiltshire, B., Shankar, K., and Michaelis, V.K. (2017). Multinuclear magnetic resonance tracking of hydro, thermal, and hydrothermal decomposition of  $\text{CH}_3\text{NH}_3\text{PbI}_3$ . *J. Phys. Chem. C* *121*, 1013–1024.
- Bi, E., Chen, H., Xie, F., Wu, Y., Chen, W., Su, Y., Islam, A., Grätzel, M., Yang, X., and Han, L. (2016). Diffusion engineering of ions and charge carriers for stable efficient perovskite solar cells. *Nat. Commun.* *8*, 15330.
- Bian, H., Bai, D., Jin, Z., Wang, K., Liang, L., Wang, H., Zhang, J., Wang, Q., and Liu, S. (2018). Graded bandgap  $\text{CsPbI}_{2-x}\text{Br}_{1-x}$  perovskite solar cells with a stabilized efficiency of 14.4%. *Joule* *2*, 1–11.
- Boyd, C.C., Cheacharoen, R., Leijtens, T., and McGehee, M.D. (2019). Understanding degradation mechanisms and improving stability of perovskite photovoltaics. *Chem. Rev.* *119*, 3418–3451.
- Chen, H., Fu, W., Huang, C., Zhang, Z., Li, S., Ding, F., Shi, M., Li, C.-Z., Jen, A.K.-Y., and Chen, H. (2017). Molecular engineered hole-extraction materials to enable dopant-free, efficient p-i-n perovskite solar cells. *Adv. Energy Mater.* *7*, 1700012.
- Chen, J., Zuo, L., Zhang, Y., Lian, X., Fu, W., Yan, J., Li, J., Wu, G., Li, C.-Z., and Chen, H. (2018). High-performance thickness insensitive perovskite solar cells with enhanced moisture stability. *Adv. Energy Mater.* *8*, 1800438.
- Deng, Y., Zheng, X., Bai, Y., Wang, Q., Zhao, J., and Huang, J. (2018). Surfactant-controlled ink drying enables high-speed deposition of perovskite films for efficient photovoltaic modules. *Nat. Energy* *3*, 560–566.
- Deretzis, I., Alberti, A., Pellegrino, G., Smecca, E., Giannazzo, F., Sakai, N., Miyasaka, T., and Magna, A.L. (2015). Atomistic origins of  $\text{CH}_3\text{NH}_3\text{PbI}_3$  degradation to  $\text{PbI}_2$  in vacuum. *Appl. Phys. Lett.* *106*, 131904.
- Deretzis, I., Smecca, E., Mannino, G., La Magna, A., Miyasaka, T., and Alberti, A. (2018). Stability and degradation in hybrid perovskites: is the glass half-empty or half-full? *J. Phys. Chem. Lett.* *9*, 3000–3007.
- Fabini, D.H., Stoumpos, C.C., Laurita, G., Kaltzoglou, A., Kontos, A.G., Falaras, P., Kanatzidis, M.G., and Seshadri, R. (2016). Reentrant structural and optical properties and large positive thermal expansion in perovskite formamidinium lead iodide. *Angew. Chem. Int. Ed.* *55*, 15392–15396.
- Han, Y., Meyer, S., Dkhissi, Y., Weber, K., Pringle, J.M., Bach, U., Spiccia, L., and Cheng, Y.-B. (2015). Degradation observations of encapsulated planar  $\text{CH}_3\text{NH}_3\text{PbI}_3$  perovskite solar cells at high temperatures and humidity. *J. Mater. Chem. A* *3*, 8139–8147.
- Hu, X., Meng, X., Zhang, L., Zhang, Y., Cai, Z., Huang, Z., Su, M., Wang, Y., Li, M., Li, F., et al. (2019). A mechanically robust conducting polymer network electrode for efficient flexible perovskite solar cells. *Joule* *3*, 1–14.
- Huang, C., Fu, W., Li, C.-Z., Zhang, Z., Qiu, W., Shi, M., Heremans, P., Jen, A.K.Y., and Chen, H. (2016). Dopant-free hole-transporting material with a C3h symmetrical truxene core for highly efficient perovskite solar cells. *J. Am. Chem. Soc.* *138*, 2528–2531.
- Jacobsson, T.J., Schwan, L.J., Ottosson, M., Hagfeldt, A., and Edvinsson, T. (2015). Determination of thermal expansion coefficients and locating the temperature-induced phase transition in methylammonium lead perovskites using X-ray diffraction. *Inorg. Chem.* *54*, 10678–10685.
- Jiang, Q., Zhao, Y., Zhang, X., Yang, X., Chen, Y., Chu, Z., Ye, Q., Li, X., Yin, Z., and You, J. (2019a). Surface passivation of perovskite film for efficient solar cells. *Nat. Photon.* *13*, 460–466.
- Jiang, Y., Qiu, L., Juarez-Perez, E.J., Ono, L.K., Hu, Z., Liu, Z., Wu, Z., Meng, L., Wang, Q., and Qi, Y. (2019b). Reduction of lead leakage from damaged lead halide perovskite solar modules using self-healing polymer-based encapsulation. *Nat. Energy* *4*, 585–593.
- Juarez-Perez, J.E., Hawash, Z., Raga, R.S., Ono, K.L., and Qi, Y. (2016). Thermal degradation of  $\text{CH}_3\text{NH}_3\text{PbI}_3$  perovskite into  $\text{NH}_3$  and  $\text{CH}_3\text{I}$  gases observed by coupled thermogravimetry–mass spectrometry analysis. *Energy Environ. Sci.* *9*, 3406–3410.
- Jung, E.H., Jeon, N.J., Park, E.Y., Moon, C.S., Shin, T.J., Yang, T.-Y., Noh, J.H., and Seo, J. (2019). Efficient, stable and scalable perovskite solar cells using poly(3-hexylthiophene). *Nature* *567*, 511–515.
- Kojima, A., Teshima, K., Shirai, Y., and Miyasaka, T. (2009). Organometal halide perovskites as visible-light sensitizers for photovoltaic cells. *J. Am. Chem. Soc.* *131*, 6050–6051.
- Li, J., Munir, R., Fan, Y., Niu, T., Liu, Y., Zhong, Y., Yang, Z., Tian, Y., Liu, B., Sun, J., et al. (2018). Phase transition control for high-performance blade-coated perovskite solar cells. *Joule* *2*, 1313–1330.
- Liu, L., Huang, S., Lu, Y., Liu, P., Zhao, Y., Shi, C., Zhang, S., Wu, J., Zhong, H., Sui, M., et al. (2018). Grain-boundary “patches” by in situ conversion to enhance perovskite solar cells stability. *Adv. Mater.* *30*, 1800544.
- Niu, T., Lu, J., Munir, R., Li, J., Barrit, D., Zhang, X., Hu, H., Yang, Z., Amassian, A., Zhao, K., et al. (2018). Stable high-performance perovskite solar cells via grain boundary passivation. *Adv. Mater.* *30*, 1706576.
- Ramirez, C., Yadavalli, S.K., Garcés, H.F., Zhou, Y., and Padture, N.P. (2018). Thermo-mechanical behavior of organic-inorganic halide perovskites for solar cells. *Scr. Mater.* *150*, 36–41.
- Reyes-Martinez, M.A., Abdelhady, A.L., Saidaminov, M.I., Chung, D.Y., Bakr, O.M.,

- Kanatzidis, M.G., Soboyejo, W.O., and Loo, Y.-L. (2017). Time-dependent mechanical response of  $\text{APbX}_3$  (A = Cs,  $\text{CH}_3\text{NH}_3$ ; X = I, Br) single crystals. *Adv. Mater.* **29**, 1606556.
- Rolston, N., Watson, B.L., Bailie, C.D., McGehee, M.D., Bastos, J.P., Gehlhaar, R., Kim, J.-E., Vak, D., Mallajosyula, A.T., Gupta, G., et al. (2016). Mechanical integrity of solution-processed perovskite solar cells. *Extreme Mech. Lett.* **9**, 353–358.
- Rolston, N., Bush, K.A., Printz, A.D., Gold-Parker, A., Ding, Y., Toney, M.F., McGehee, M.D., and Dauskardt, R.H. (2018a). Engineering stress in perovskite solar cells to improve stability. *Adv. Energy Mater.* **8**, 1802139.
- Rolston, N., Printz, A.D., Tracy, J.M., Weerasinghe, H.C., Vak, D., Haur, L.J., Priyadarshi, A., Mathews, N., Slotcavage, D.J., McGehee, M.D., et al. (2018b). Effect of cation composition on the mechanical stability of perovskite solar cells. *Adv. Energy Mater.* **8**, 1702116.
- Smecca, E., Numata, Y., Deretzis, I., Pellegrino, G., Boninelli, S., Miyasaka, T., La Magna, A., and Alberti, A. (2016). Stability of solution-processed  $\text{MAPbI}_3$  and  $\text{FAPbI}_3$  layers. *Phys. Chem. Chem. Phys.* **18**, 13413–13422.
- Tress, W., Domanski, K., Carlsen, B., Agarwalla, A., Alharbi, E.A., Grätzel, M., and Hagfeldt, A. (2019). Performance of perovskite solar cells under simulated temperature-illumination real-world operating conditions. *Nat. Energy* **4**, 568–574.
- Turren-Cruz, S.H., Hagfeldt, A., and Saliba, M. (2018). Methylammonium-free, high-performance, and stable perovskite solar cells on a planar architecture. *Science* **362**, 449–453.
- Wang, Y., Wu, T., Barbaud, J., Kong, W., Cui, D., Chen, H., Yang, X., and Han, L. (2019). Stabilizing heterostructures of soft perovskite semiconductors. *Science* **365**, 687–691.
- Wu, C.-G., Chiang, C.-H., Tseng, Z.-L., Nazeeruddin, M.K., Hagfeldt, A., and Grätzel, M. (2015). High efficiency stable inverted perovskite solar cells without current hysteresis. *Energy Environ. Sci.* **8**, 2725–2733.
- Yang, W., Chen, J., Lian, X., Li, J., Yao, F., Wu, G., Qiu, W., Jin, C., Heremans, P., and Chen, H. (2019). Black phosphorus quantum dots induced high-quality perovskite film for efficient and thermally stable planar perovskite solar cells. *Solar RRL* **3**, 1900132.
- Yu, X., Qin, Y., and Peng, Q. (2017). Probe decomposition of methylammonium lead iodide perovskite in  $\text{N}_2$  and  $\text{O}_2$  by in situ infrared spectroscopy. *J. Phys. Chem. A* **121**, 1169–1174.
- Zhao, J., Deng, Y., Wei, H., Zheng, X., Yu, Z., Shao, Y., Shield, J.E., and Huang, J. (2017). Strained hybrid perovskite thin films and their impact on the intrinsic stability of perovskite solar cells. *Sci. Adv.* **3**, eaao5616.
- Zhou, H., Chen, Q., Li, G., Luo, S., Song, T.-b., Duan, H.-S., Hong, Z., You, J., Liu, Y., and Yang, Y. (2014). Interface engineering of highly efficient perovskite solar cells. *Science* **345**, 542–546.
- Zuo, L., Gu, Z., Ye, T., Fu, W., Wu, G., Li, H., and Chen, H. (2015). Enhanced photovoltaic performance of  $\text{CH}_3\text{NH}_3\text{PbI}_3$  perovskite solar cells through interfacial engineering using self-assembling monolayer. *J. Am. Chem. Soc.* **137**, 2674–2679.
- Zuo, L., Chen, Q., De Marco, N., Hsieh, Y.-T., Chen, H., Sun, P., Chang, S.-Y., Zhao, H., Dong, S., and Yang, Y. (2017). Tailoring the interfacial chemical interaction for high-efficiency perovskite solar cells. *Nano Lett.* **17**, 269–275.

**ISCI, Volume 22**

**Supplemental Information**

**Toward Highly Thermal Stable  
Perovskite Solar Cells by Rational  
Design of Interfacial Layer**

**Weitao Yang, Danming Zhong, Minmin Shi, Shaoxing Qu, and Hongzheng Chen**

## Transparent Methods

### Experimental Procedures

**Materials:** Dimethyl sulfoxide (DMSO), N,N-dimethylformamide (DMF),  $\text{PbI}_2$  were purchased from TCI. Chlorobenzene (CB), ethanol, isopropanol (IPA), and toluene were bought from Sigma Aldrich. 15%  $\text{SnO}_2$  colloid solution in water, 4-tert-butylpyridine (tBP), abis(trifluoromethylsulfonyl)amine lithium salt (Li-TFSI) and  $\text{MoO}_3$  were purchased from Alfa Aesar. Bathocuproine (BCP), [6,6]-phenyl-C61-butyric acid methyl ester (PCBM), Poly[bis(4-phenyl)(2,4,6-trimethylphenyl)amine] (PTAA) were obtained from J&K., American Dye Source and Xi'an p-OLED, respectively. Methylammonium iodide (MAI) was purchased from Shanghai Mater Win New Materials. 4-Tert-butylpyridine (tBP) and bis(trifluoromethylsulfonyl)amine lithium salt (Li-TFSI) were purchased from Alfa Aesar. All materials were used without further purification.  $\text{TiO}_2$  nanocrystal were synthesized based on the procedure reported by Yang Y. et al (Zhou et al., 2014).

**Device Fabrication and Characterization:** Perovskite solar cells were fabricated on glass substrates pre-coated with a layer of indium tin oxides (ITO). The ITO substrates were cleaned sequentially by detergent, deionized water, acetone, and isopropanol for 15 min in an ultrasonic bath before fabrication. The pre-cleaned ITO substrates were then treated with UV-Ozone for 20 min. To deposit the  $\text{SnO}_2$  layer, 15%  $\text{SnO}_2$  colloid solution was diluted by deionized water to 5% and thereafter spun coat onto ITO substrates at 3500 revolutions per minute (rpm) for 45 s, followed by thermal annealing in air at 150 °C for 30 min. To deposit the  $\text{TiO}_2$  layer,  $\text{TiO}_2$  nanocrystal solution was spun coat onto ITO substrates at 3500 rpm for 45 s, followed by thermal annealing in air at 150 °C for 30 min. To deposit the PEDOT:PSS layer, PEDOT:PSS (Baytron P Al4083) was filtered through a polytetrafluoroethylene filter (0.45  $\mu\text{m}$ ) and thereafter spun coat onto ITO substrates at 3500 rpm for 45 s, followed by baking at 140 °C for 20 min. To deposit the thin PEDOT:PSS layer, PEDOT:PSS was diluted 4 times by deionized water and filtered through a polytetrafluoroethylene filter (0.45  $\mu\text{m}$ ), and then spun coat onto

ITO substrates at 3500 rpm for 45 s, followed by baking at 140 °C for 20 min to get a ~8 nm PEDOT:PSS thin film. To deposit the thin PTAA layer, the ITO substrates were transferred to a glovebox. Then a layer of PTAA (2 mg mL<sup>-1</sup> in toluene) was spin-coated onto the cleaned ITO at 6000 rpm for 45 s. To deposit thick PTAA layer, a solution dissolved in 1 mL of toluene contained 15 mg of PTAA, 7.5 μL of LiTFSI stock solution (520 mg/mL in acetonitrile) and 7.5 μL of tBP. The PTAA solution was spun onto the perovskite film at 4000 rpm for 30 s to get a ~30 nm PTAA thick film. To deposit PEDOT:PSS/PTAA bilayer, PEDOT:PSS was diluted 2 times by deionized water and filtered through a polytetrafluoroethylene filter (0.45 μm), and then spun coat onto ITO substrates at 3500 rpm for 45 s, followed by baking at 140 °C for 20 min to get a ~15 nm PEDOT:PSS thin film. The pre-deposited substrates were then transferred to a glovebox and a layer of PTAA with thickness of 7 nm (2 mg mL<sup>-1</sup> in toluene) was spin-coated onto them at 6000 rpm for 45 s.

Deposition of SAM follows previous literature (Zuo et al., 2017). In brief, isonicotinic acid was dissolved in methanol at a concentration of 0.5mg/mL, and was then spun onto the MO-based substrates at 3000 rpm. They were then annealed at 120°C for 15 min. Afterward, excessive isonicotinic acid was washed away by methanol.

PbI<sub>2</sub>(DMSO) was dissolved in DMF at a concentration of 1 M. MAI was dissolved in IPA at a concentration of 50 mg mL<sup>-1</sup>. To make the perovskite film, the PbI<sub>2</sub>(DMSO) solution was spin coted onto the substrates with different interfacial layers at 3000 rpm for 30s, immediately followed by spin coating of MAI solution at 3000 rpm for another 30 s. Afterward, the obtained film were annealed at 90°C for 15 min. PCBM/BCP (or PTAA/MoO<sub>3</sub>) charge transport layers were then deposited on the top of MAPbI<sub>3</sub> film to form structures of ITO/HTL/MAPbI<sub>3</sub>/PCBM/BCP/Ag (or ITO/ETL/MAPbI<sub>3</sub>/PTAA/MoO<sub>3</sub>/Ag) following steps described below. (i) PCBM solution (20 mg mL<sup>-1</sup> in CB) was then spin-coated onto the perovskite film at 2000 rpm for 30 s, followed by the spin-coating of a BCP solution (0.5 mg mL<sup>-1</sup> in ethanol) at 3000 rpm for 30 s. After this, the samples were transfer to the vacuum chamber for the deposition of 100 nm Ag (or Au) under a high vacuum of 5 × 10<sup>-4</sup> Pa. (ii) PTAA was deposited from a solution dissolved in 1 mL of toluene contained 15 mg of PTAA, 7.5 μL of LiTFSI stock

solution (520 mg/mL in acetonitrile) and 7.5  $\mu\text{L}$  of tBP. The PTAA solution was spun onto the perovskite film at 4000 rpm for 30 s. Finally, a 10 nm  $\text{MoO}_3$  and 100 nm silver (Ag) were thermally evaporated under vacuum, respectively.

The X-ray diffraction patterns were recorded at a scan rate of  $10^\circ \text{ min}^{-1}$  on Rigaku Ultima IV X-ray diffractometer with Cu  $\text{K}\alpha$  radiation (0.15406 nm). The current density-voltage ( $J$ - $V$ ) curves of the devices were measured in glovebox with Keithley 2400 measurement source units under 1 sun, AM 1.5 G spectra from a solar simulator (Taiwan, Enlitech), and the light intensity was calibrated with a standard silicon photovoltaic reference cell. The voltage step is 0.02 V, with a delay time of 10 ms per step, the total scanning rate is  $0.095 \text{ V s}^{-1}$ . For devices thermal stability test, devices were placed on  $100^\circ\text{C}$  hotplate in glovebox. During the aging period, the devices were taken off the hotplate and cooled to room temperature from time to time for PCE decay tracing. Optical microscope images were taken via Nikon LV100 POL equipped with a digital camera.

### **Mechanics Simulation**

Finite Element Method (Abaqus/Standard) is used to simulate the mechanical behaviours of the PVSCs and 3D solid parts are adopted to represent the  $\text{MAPbI}_3$ , interfacial layer and ITO. We use the 'Tie' constraint to connect two separate surfaces of two various parts together, and there is no relative motion between the two surfaces. The mechanical properties of each part, including the elastic modulus and thermal expansion coefficient, are listed in Table S1, and the lengths and widths are set as  $1000 \text{ nm} \times 1000 \text{ nm}$ , with the thickness of each layer set as Table S1. An 8-node linear element with reduced integration and hourglass control (C3D8R) is chosen. Along the thickness direction, there are at least 4 layers of elements for each part to ensure the calculation accuracy.

The bottom surface of PVSC (the ITO layer in our simulation) is fixed, in other words, six degrees of freedom of the bottom surface (three of displacements and three of rotations) are fixed, to prevent the PVSC from rigid body translation. The other surfaces of the PVSC are free to deformation. A predefined temperature field with

initial magnitude 20°C is applied, then modified to 120°C, which is consistent with our experiment. Finally, the Tresca equivalent stress field and deformation field ( $\epsilon_{11}$ ) of MAPbI<sub>3</sub> part are exported for further analysis. In our simulation, direction 1 and direction 2 are along the length and width directions respectively, so they reflect the in-plane stress and strain. Due to the symmetry of PVSC structure, the strains along direction 1 are equivalent to their counterparts along direction 2, so we adopt  $\epsilon_{11}$  in this work to show the in-plane deformation.

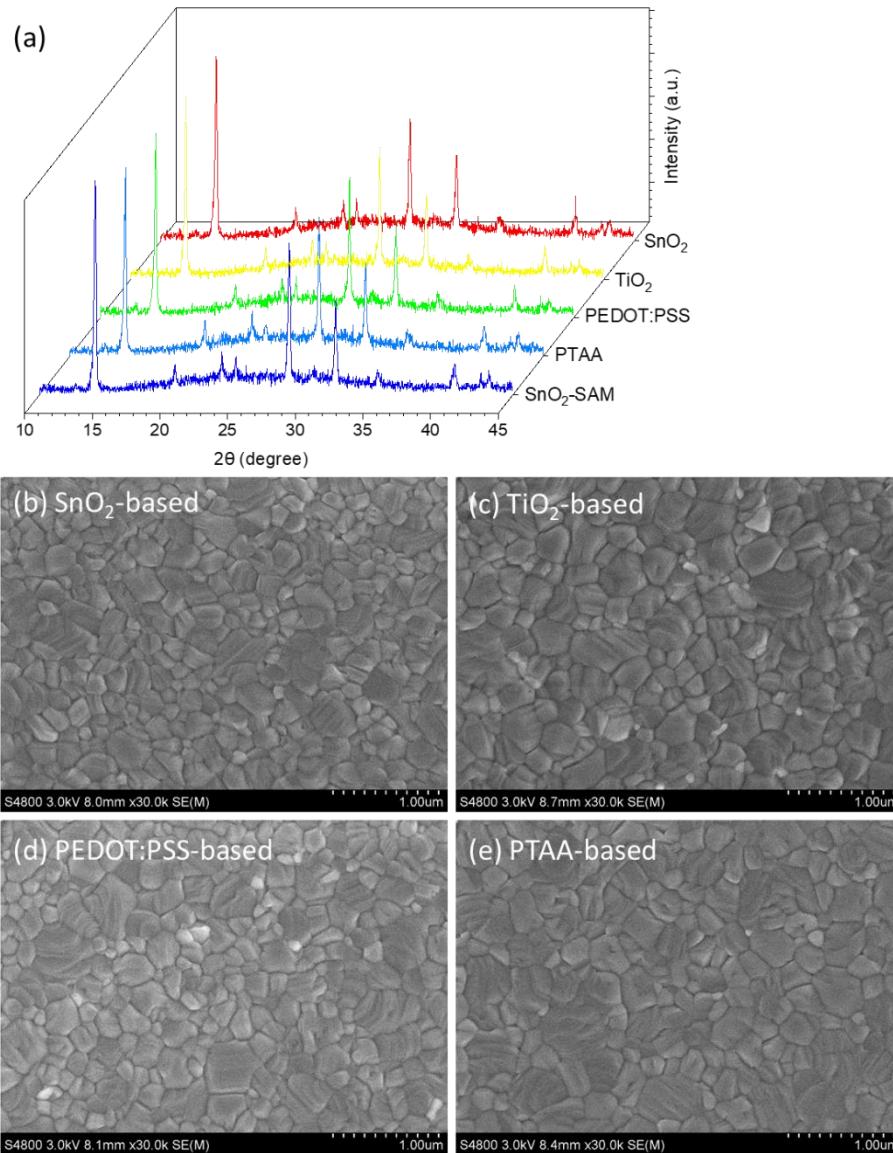


Figure S1. (a) XRD patterns and (b)-(e) SEM images of different perovskite films. Related to Figure 2.

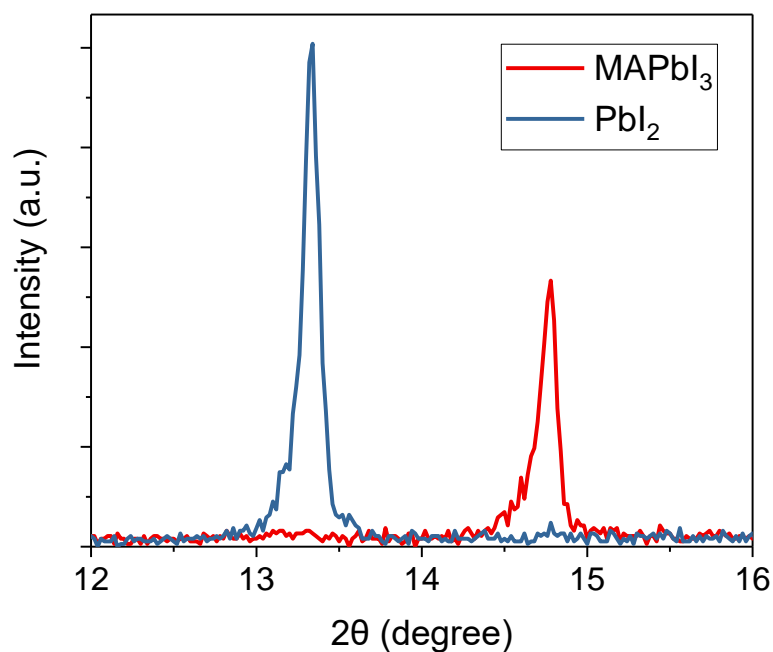


Figure S2. XRD patterns of fresh perovskite film (red line) and totally aged perovskite film (blue line). Related to Figure 2.

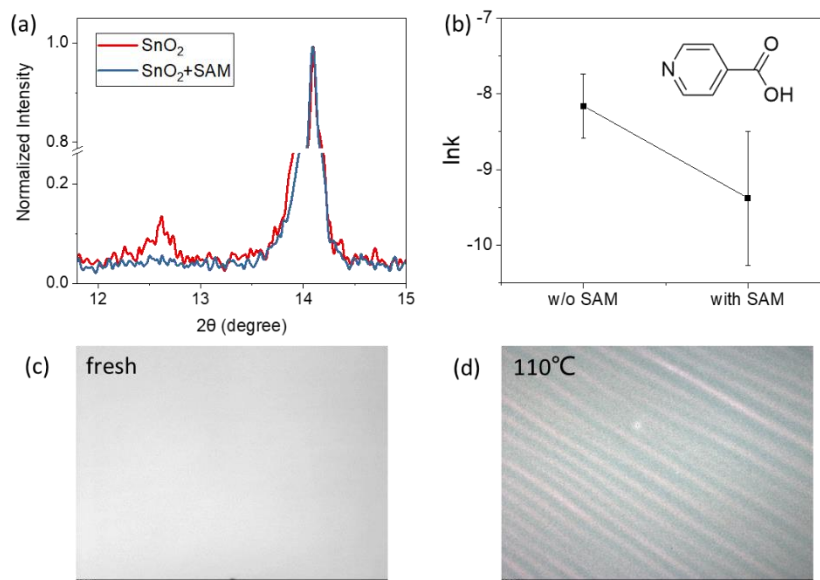


Figure S3. (a) XRD patterns of aged perovskite films based on  $\text{SnO}_2$  (red line) and  $\text{SnO}_2$ -SAM (blue line). (b)  $\ln k$  of perovskite films on MOs interfacial layers without and with SAM passivation. The inset is the molecular structure of the SAM molecule. Optical microscope images of  $\text{SnO}_2$ -based perovskite (c) before and (d) after thermal aging at

110 °C. Related to Figure 2.

Table S1. Summary of mechanical parameters involved in the mechanics simulation.

Related to Figure 4.

layers	Young's modulus (GPa)	Thickness (nm)
MAPbI <sub>3</sub>	10~12 (Sun et al., 2015)	300
PEDOT:PSS	1~3 (Lang et al., 2009; Okuzaki et al., 2003)	20
PTAA	~1 (Lee et al., 2019)	5
ITO	118 (Park et al., 2003)	100
SnO <sub>2</sub> , TiO <sub>2</sub>	>150 (Borgese et al., 2012; Zheng et al., 2011)	20
Metal electrode	6~12	100
PCBM	2 (Awartani et al., 2013)	20

Poisson ratio is set to be 0.3. The thermal expansion coefficient of MAPbI<sub>3</sub> is  $157 \times 10^{-6} \text{ K}^{-1}$ . Due to the small thermal expansion coefficient and large elastic modulus, both the thermal-induced deformation and mechanical-induced deformation of ITO layer are negligible. And the thermal expansion coefficient of other layers is set to be  $50 \times 10^{-6} \text{ K}^{-1}$ .

1.

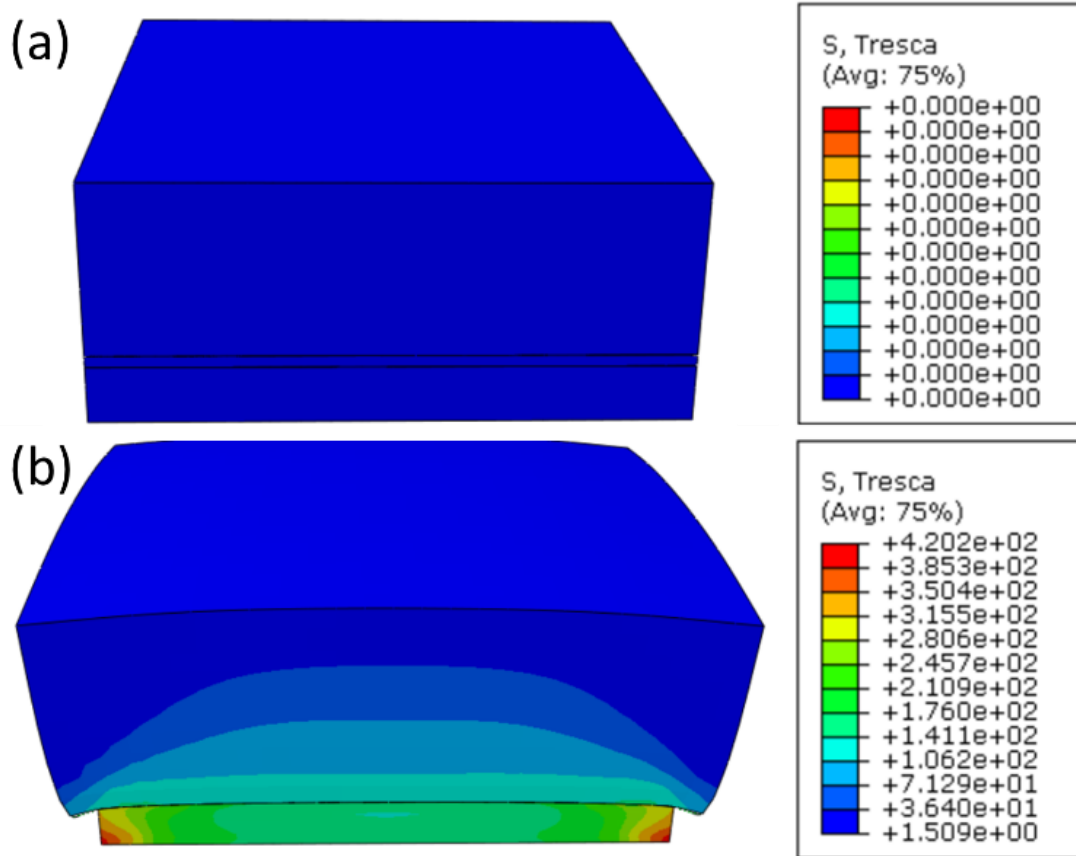


Figure S4. Perovskite film (a) before and (b) after applying temperature field. A deformation scale factor of 10 is used to make the deformation of PVSC obvious. Related to Figure 4.

Because of the constraint effect of substrate on perovskite film, the inner surface of perovskite film is stopped from expansion, whereas the outer surface of perovskite film is rather free to expand. These introduce unbalanced strain within the perovskite film across the thickness direction.

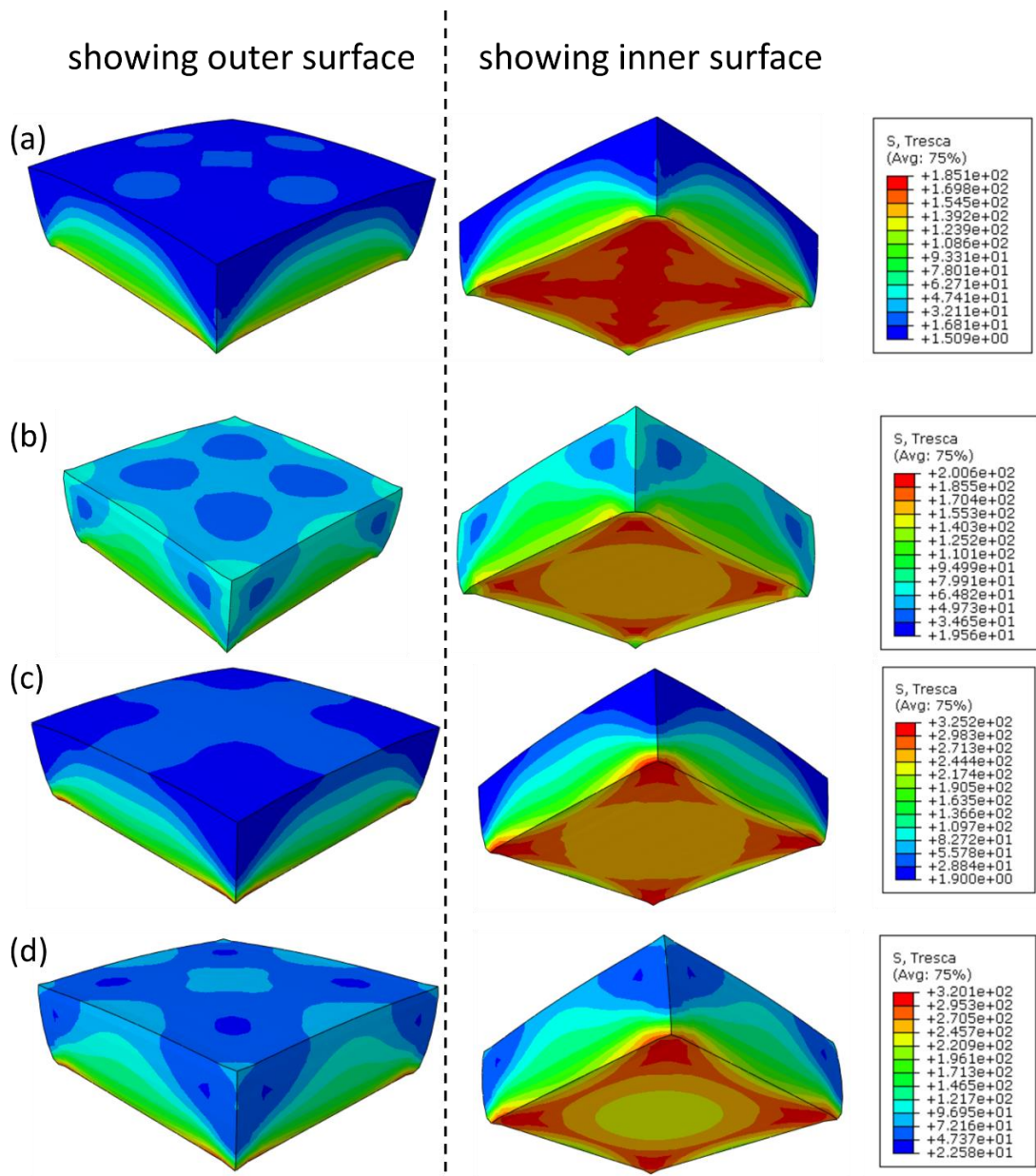


Figure S5. Thermal-induced Tresca stress distribution of perovskite films on interlayer with modulus of 1.5 GPa (a) without and (b) with PCBM layer and counter electrode. Tresca stress distribution of perovskite films on interlayer with modulus of 48 GPa (c) without and (d) with PCBM layer and counter electrode. A deformation scale factor of 10 is used to make the deformation of PVSC obvious. Related to Figure 4.

Herein, increased Tresca stress are observed in both perovskite films without and with counter interfacial layer and electrode when the modulus of interfacial layer increases (from 1.5 GPa to 48 GPa). These results indicate that our conclusion deduced from the simulation based on ITO/interfacial layer/perovskite half device could be extended to that on full device.

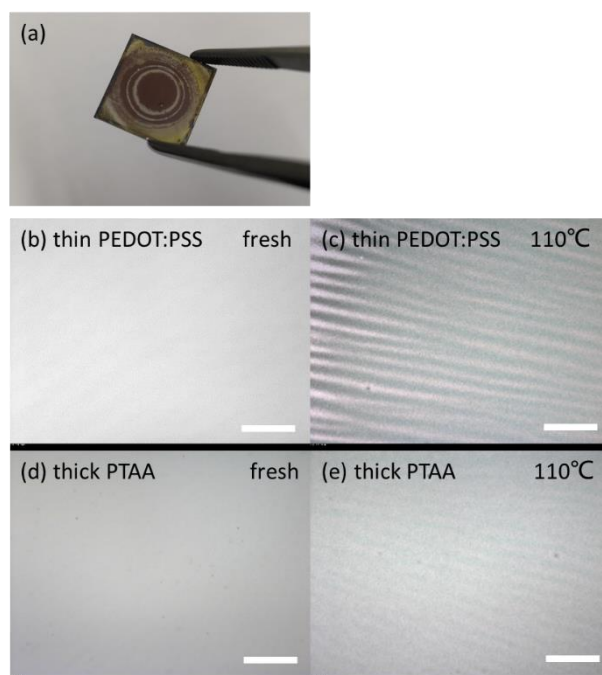


Figure S6. (a) MAPbI<sub>3</sub> prepared on thick PTAA based substrate. The thickness of PTAA is ~30 nm. (b)-(e) Optical microscope images of perovskite films deposited on different interfacial layers under thermal aging with different temperatures. Scale-bars in all pictures represent 200 μm. Related to Figure 4.

Table S2. Photovoltaic parameters of PVSCs based on different interfacial layers under the illumination of AM 1.5 G, 100 mW/cm<sup>2</sup>. The average values are calculated from 8 devices. Related to Figure 5.

Interfacial layer	V <sub>oc</sub> (V)	J <sub>sc</sub> (mA/cm <sup>2</sup> )	FF	PCE (%)
SnO <sub>2</sub>	1.07	21.56	0.66	15.26 (14.73±0.48)
TiO <sub>2</sub>	1.07	22.25	0.57	13.55 (12.24±1.13)
PEDOT:PSS	1.01	19.33	0.70	13.56 (12.90±0.68)
PTAA	1.07	22.22	0.75	17.83 (16.74±0.91)
TPL	1.08	22.46	0.76	18.78 (17.18±1.00)

Table S3. Optimization of the TPL by varying the thickness of PEDOT:PSS and PTAA, respectively. Photovoltaic parameters of PVSCs are taken under the illumination of AM 1.5 G, 100 mW/cm<sup>2</sup>. The average values are calculated from 8 devices. Related to Figure 5.

Thickness (nm)		$V_{oc}$ (V)	$J_{sc}$ (mA/cm <sup>2</sup> )	FF	PCE (%)
PEDOT:PSS	PTAA				
24	7	1.02	18.13	0.76	14.03 (13.94±0.09)
	3	1.02	18.33	0.78	14.68 (13.85±0.68)
14	7	1.08	22.46	0.76	18.78 (17.18±1.00)
	3	0.97	19.79	0.74	14.39 (13.87±0.49)
12	7	1.07	21.73	0.74	17.49 (16.94±0.52)
	3	0.98	19.78	0.74	14.38 (13.63±0.47)

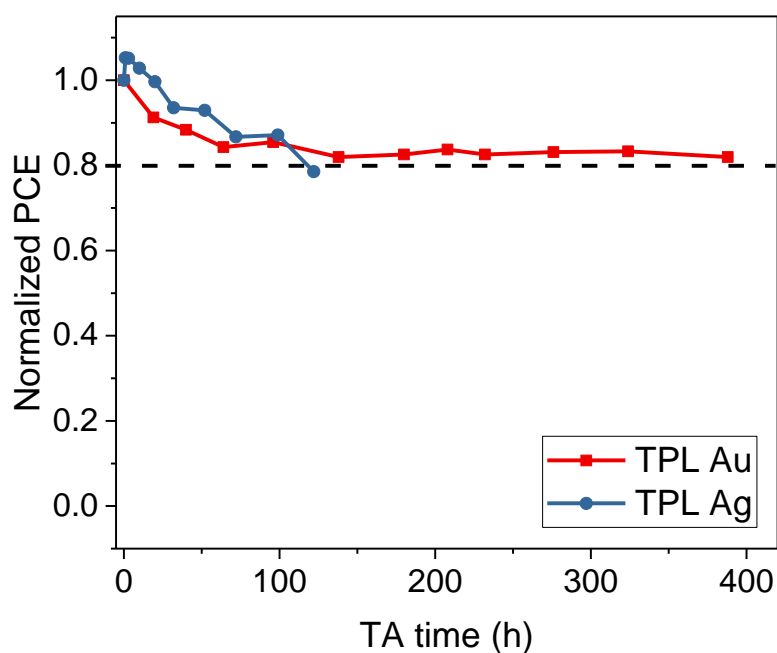


Figure S7. PCE evolution of PVSCs based on TPL with Ag (blue line) and Au (red line) electrode heated at 100°C in glovebox. Related to Figure 5.

## References

- Zhou, H., Chen, Q., Li, G., Luo, S., Song, T.-b., Duan, H.-S., Hong, Z., You, J., Liu, Y., and Yang, Y. (2014). Interface engineering of highly efficient perovskite solar cells. *Science* *345*, 542-546.
- Zuo, L., Chen, Q., De Marco, N., Hsieh, Y.-T., Chen, H., Sun, P., Chang, S.-Y., Zhao, H., Dong, S., and Yang, Y. (2017). Tailoring the interfacial chemical interaction for high-efficiency perovskite solar cells. *Nano Lett.* *17*, 269-275.
- Sun, S., Fang, Y., Kieslich, G., White, T. J., and Cheetham, A. K. (2015). Mechanical properties of organic–inorganic halide perovskites,  $\text{CH}_3\text{NH}_3\text{PbX}_3$  ( $X = \text{I}, \text{Br}$  and  $\text{Cl}$ ), by nanoindentation. *J. Mater. Chem. A* *3*, 18450-18455.
- Lang, U., Naujoks, N., and Dual, J. (2009). Mechanical characterization of PEDOT:PSS thin films. *Synth. Met.* *159*, 473-479.
- Okuzaki, H., and Ishihara, M. (2003). Spinning and characterization of conducting microfibers. *Macromol. Rapid Commun.* *24*, 261-264.
- Lee, I., Rolston, N., Brunner, P.-L., and Dauskardt, R. H. (2019). Hole-transport layer molecular weight and doping effects on perovskite solar cell efficiency and mechanical behavior. *ACS Appl. Mater. Interfaces* *11*, 23757-23764.
- Park, S. K., Han, J. I., Moon, D. G., and Kim, W. K. (2003). Mechanical stability of externally deformed indium–tin–oxide films on polymer substrates. *Jpn. J. Appl. Phys.* *42*, 623-629.
- Borgese, L., Gelfi, M., Bontempi, E., Goudeau, P., Geandier, G., Thiaudière, D., and Depero, L. E. (2012). Young modulus and Poisson ratio measurements of  $\text{TiO}_2$  thin films deposited with Atomic Layer Deposition. *Surf. Coat. Technol.* *206*, 2459-2463.
- Zheng, Y., and Geer, R. E. (2011). Nanomechanical imaging and nanoscale elastic modulus measurements of  $\text{SnO}_2$  nanobelts. *MRS Proceedings* *821*, P2.3.
- Awartani, O., Lemanski, B. I., Ro, H. W., Richter, L. J., DeLongchamp, D. M., and O'Connor, B. T. (2013). Correlating stiffness, ductility, and morphology of polymer:fullerene films for solar cell applications. *Adv. Energy Mater.* *3*, 399-406.